Potential of the solid-Earth response for limiting long-term West Antarctic Ice Sheet retreat in a warming climate

Hannes Konrad [a,b,c,*,1], Ingo Sasgen [a,d], David Pollard [e], Volker Klemann [a]

[a] *Helmholtz Centre Potsdam, German Research Centre for Geosciences GFZ, Section 1.3: Earth System Modelling, Telegrafenberg, D-14473 Potsdam, Germany*
[b] *Alfred Wegener Institute, Helmholtz Centre for Polar and Marine Research, Bremerhaven, Germany*
[c] *Free University of Berlin, Department of Earth Sciences, Institute of Meteorology, Berlin, Germany*
[d] *Department of Geosciences, Pennsylvania State University, University Park, PA, USA*
[e] *Earth and Environmental Systems Institute, Pennsylvania State University, University Park, PA, USA*

ARTICLE INFO

ABSTRACT

We employ a coupled model for ice-sheet dynamics and Maxwell viscoelastic solid-Earth dynamics, including a gravitationally consistent description of sea level. With this model, we study the influence of the solid Earth on the future evolution of the West Antarctic Ice Sheet (WAIS). Starting from steady-state conditions close to the present-day configuration of the Antarctic Ice Sheet, we apply different atmospheric and oceanic forcings and solid-Earth rheologies in order to analyse the retreat of the WAIS. Climate forcing is the primary control on the occurrence of WAIS collapse. For moderate climate forcing and weak solid-Earth rheologies, however, we find that the relative sea level (RSL) fall associated with the viscoelastic solid-Earth response due to unloading by WAIS retreat limits the retreat to the Amundsen Sea embayment on time scales of several millennia, whereas stiffer Earth structures yield a collapse under these conditions. Under stronger climate forcing, weak Earth structures associated with the West Antarctic rift system produce a delay of up to 5000 years in comparison to stiffer, Antarctic-average solid-Earth rheologies. Furthermore, we find that sea-level rise from an assumed fast deglaciation of the Greenland Ice Sheet induces WAIS collapse in the presence of higher asthenosphere viscosities in cases when the climatic forcing is too weak to force WAIS collapse alone.

© 2015 Elsevier B.V. All rights reserved.

1. Introduction

The West Antarctic Ice Sheet (WAIS) is largely grounded below sea level on an inward deepening bed (Fretwell et al., 2013). This setting makes it susceptible to the Marine Ice Sheet Instability (MISI) mechanism (Thomas and Bentley, 1978; Schoof, 2007): The retreat of grounded ice implies higher ice transport into the ice shelves due to increasing cross sectional area along the grounding line (GL). This leads to runaway loss of ice grounded below sea level. Geological observations suggest much smaller WAIS volumes in past interglacials (Mercer, 1968; Scherer et al., 1998). The question of future instability, rapid deglaciation and related sea-level contribution of the WAIS is a major concern (Clark and Lingle, 1977; Oppenheimer, 1998; Joughin and Alley, 2011).

There have been many recent studies addressing the current extent of mass loss in the Amundsen Sea embayment (King et al., 2012; Rignot et al., 2014; Sutterley et al., 2014) which find that the WAIS has undergone a strong loss of ice along the Amundsen Sea coast in the past years to decades. Geologic studies have found evidence of ice loss in this area during earlier stages of the Holocene (Hillenbrand et al., 2013). Favier et al. (2014) find that Pine Island Glacier in the Amundsen Sea embayment is retreating mainly due to MISI and will continue to do so for the next several decades at least.

A retreating ice sheet unloads the underlying solid Earth, which responds by instantaneous elastic and delayed viscoelastic deformation (Peltier, 1974) and by falling sea surface heights as the gravitational attraction of ocean waters by the shrinking ice mass is diminished. This is manifested as a decrease of ocean depth, or relative sea level (RSL), in the vicinity of the ice sheet. Consequently, the Earth's response provides a negative feedback on GL retreat (Gomez et al., 2010, 2012). In particular, Gomez et al. (2012) found in idealized numerical experiments that the described decrease in ocean depth (or RSL fall) may stabilize an ice sheet undergoing MISI. Adhikari et al. (2014) demonstrated in de-

---

tail how the bedrock uplift and the associated change of bedrock slopes in response to retreat of the Antarctic Ice Sheet (AIS) decrease the driving stress in the ice body and thereby stabilize the ice sheet. In a specific scenario such as WAIS retreat in a warming climate, the impact of this negative feedback should depend on the time scales of the viscoelastic deformation and therefore on the viscosity structure of the solid Earth.

The tectonic structure of Antarctica and the West Antarctic rift system in particular have been investigated in the past by seismic tomography and other geophysical methods. The East Antarctic Ice Sheet (EAIS) rests on a continental cratonic lithosphere and mantle (Morelli and Danesi, 2004), whereas the WAIS is situated on a rifted system with possibly much lower values of elastic lithosphere thickness and asthenosphere viscosity (Behrendt, 1999; Accardo et al., 2014) and associated high geothermal heat flux and subglacial volcanism, specifically in the Amundsen Sea embayment and Marie Byrd Land (Lough et al., 2013). A relatively weak asthenosphere and thin lithosphere in the West Antarctic rift system will produce a faster viscoelastic response of the solid Earth to a change in the surface load. Therefore, the tectonic setting in West Antarctica has the potential to play a crucial role in the long-term future evolution of the WAIS.

Interactions between ice sheets and the solid Earth have been studied by Le Meur and Huybrechts (1996), Crucifix et al. (2001), van den Berg et al. (2008), Gomez et al., (2012, 2013) and de Boer et al. (2014). As in the latter three studies, we employ a coupled ice-sheet/sea-level model that accounts for viscoelastic deformation of the solid Earth, to investigate if the tectonic setting of the West Antarctic rift system, represented by radially symmetric viscosity distributions, can provide stability to the WAIS in a warming climate on time scales of several millennia. The stabilizing feedback only acts if the Earth response reaches a certain magnitude, which takes several 1000s of years. Therefore, our experiments cover a time span equivalent to the length of an interglacial (Augustin et al., 2004). Starting from a steady-state representation of today's AIS, we prescribe atmospheric and oceanic warming from present-day conditions, as well as sea-level rise from assumed ice loss of the Greenland Ice Sheet (GrIS) and other glaciated regions. Depending on the strength of the forcing and on the weakness of the solid Earth underlying the WAIS, we find that the response of the Earth and associated RSL fall can prevent a collapse of the WAIS, or delay it compared to simulations with stiffer Earth structures.

2. Model description and experimental set-up

2.1. Ice dynamics

We employ an established ice sheet-shelf model (ISM) (Pollard and DeConto, 2012b). This model solves for ice thickness, temperature, and velocity, using a hybrid combination of the Shallow Ice Approximation (SIA) and the Shallow Shelf Approximation (SSA) of the linear momentum balance for ice dynamics at any point, unless high basal friction lets the SSA become negligible and only SIA is considered. The ice dynamics at the GL are heuristically constrained by an analytical steady-state solution (Schoof, 2007), which has been found to adequately represent GL dynamics even at coarse horizontal resolutions (Pattyn et al., 2013; Gudmundsson, 2013). The reader is referred to Pollard and De-Conto (2012b) for an extensive description of the hybrid combination of SIA and SSA as well as the GL treatment. Here, the horizontal resolution is 40 km. Limited test simulations with a horizontal resolution of 20 km gave essentially the same results.

The BEDMAP2 dataset Fretwell et al. (2013) is used to provide present-day Antarctic bedrock topography, ice thickness, and surface elevation, S_{PD} (Fig. 1). Modern surface air temperatures, T_{PD},

A: Initial ice-sheet geometry

Ice-sheet surface elevation (km)

Ocean bathymetry (km)

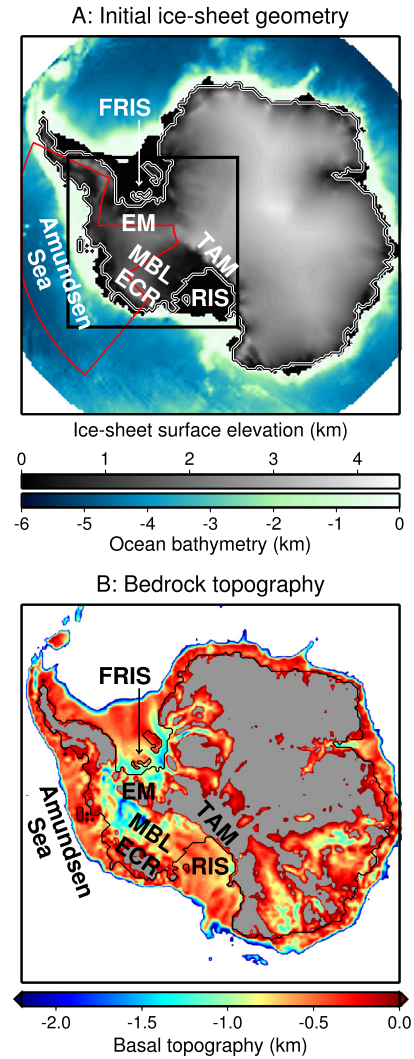**B: Bedrock topography**

Basal topography (km)

Fig. 1. A: Surface elevation of the AIS after 200 kyr of initialization (corresponding to present-day observations); the bathymetry of the surrounding ocean is also color-coded. The red line includes the Amundsen Sea Sector to which the oceanic forcing is applied. The black rectangle indicates the region of interest (Fig. 6). B: Present-day bathymetry (BEDMAP2 by Fretwell et al., 2013). Bedrock above sea level is indicated in grey. ECR: Executive Committee Range; EM: Ellsworth Mountains; FRIS: Filchner-Ronne Ice Shelf; MBL: Marie Byrd Land; RIS: Ross Ice Shelf; TAM: Transantarctic Mountains. (For interpretation of the references to color in this figure legend, the reader is referred to the web version of this article.)

and accumulation rates, $\dot{b}_{PD}$, are prescribed from observed datasets (Comiso, 2000; van de Berg et al., 2006). The applied surface temperatures, T, and accumulation rates, $\dot{b}$, are corrected for elevation changes according to

$$T = T_{PD} - \gamma \left(S - S_{PD} \right) + \Delta T_{at} \text{ and} \tag{1}$$

$$\dot{b} = \dot{b}_{PD} \times 2^{(T - T_{PD})/10\,°C} , \tag{2}$$

where S is the actual surface elevation and the lapse rate $\gamma = 0.008\,°C/m$ models the decrease of temperature with increasing surface elevation in the atmosphere. Melt-water run-off is modeled by a Positive-Degree-Day (PDD) scheme (Huybrechts and Oerlemans, 1990). The temperature offset ΔT_{at} is used in our experiments for applying the climate forcing.

Following Martin et al. (2011), the melt rates under the ice shelves $\dot{b}_s$ are parameterized as

$$\dot{b}_s = \frac{K_B K_T \rho_{oc} c_p}{\rho L} |T_{oc} - T_f| (T_{oc} - T_f) . \tag{3}$$

Here,

$$T_{oc} = T_{oc,0} + \Delta T_{oc} \qquad (4)$$

is the ocean temperature, a composite of the initial temperature $T_{oc,0}$ and a forcing offset ΔT_{oc}. The distribution of $T_{oc,0}$ is based on the data set by Levitus et al. (2012) at 400 m depth as described in the supplementary information in Pollard et al. (2015). The freezing point T_f at the lower surface of the ice shelf is given by

$$T_f = 0.0939\,°C - \frac{0.057\,°C}{PSU}\,s_{oc} - \frac{7.64 \times 10^{-4}\,°C}{m}\,z\,, \qquad (5)$$

where z is the depth below sea level of the lower ice-shelf edge (Foldvik and Kvinge, 1974). The remaining parameters in Eqs. (3) and (5) are given in the Appendix A (Table 2). Practical Salinity Units (PSU) are equivalent to 'per thousand' (‰). This parameterization does not account for hydro-fracturing or cliff failure as proposed by Pollard et al. (2015).

Iceberg calving as an ice-loss mechanism at the vertical ice–ocean interface is parameterized on the basis of upstream ice thickness and the divergence of the horizontal velocities. Another such mechanism is the melting of ice below sea level along the vertical ice–ocean interface. The treatment follows the description for melting below the ice shelves in Eq. (3) and is scaled as a surface process by the respective ice column below sea level and the respective grid cell area (Pollard and DeConto, 2012b).

As in Pollard and DeConto (2012b), geothermal heat flux is prescribed in a simple pattern with lower fluxes in East Antarctica (54.6 mW/m^2) and higher in West Antarctica (70 mW/m^2). Basal velocities are calculated from basal stresses according to a power law (Weertman, 1957). The spatial distribution of the basal friction coefficient has been inverted from present-day surface elevations by Pollard and DeConto (2012a).

The initialization of the temperature field as well as drift in an ISM are important considerations (Bindschadler et al., 2013). We opt for the steady-state initialization in order to start from a well-defined state consistent with the assumption of the solid Earth being at rest (see below). The AIS is run to a steady state for 200 kyr with fixed present-day bedrock topography and geothermal heat fluxes. The surface mass balance and the sub-shelf melt rates evolve only according to the changing ice sheet geometry ($\Delta T_{at} = \Delta T_{oc} = 0$ in Eqs. (1) and (4)). The present-day loss of Antarctic ice mass of about 71 Gt/yr (Shepherd et al., 2012) will be outweighed within a few centuries by the much higher mass losses occurring due to the prescribed climatic forcing. In the region of interest (Amundsen Sea coast and hinterland of the Ross Ice Shelf), the differences in GL position between the modeled and the observed present-day states are two grid points at maximum, and only at a few locations (Supplement S.1). The WAIS ice thicknesses differ by less than 90 m on average. Therefore, we consider the steady state as a reasonable approximation for the perturbation experiments investigated here.

2.2. Solid-Earth dynamics and sea level

As described in Konrad et al. (2014), we employ the self-gravitating viscoelastic Earth model (SGVEM) developed by Martinec (2000). It solves the equations for mass continuity and linearized linear momentum balance as well as the Poisson equation for the incremental gravitational potential for an incompressible, spherical, Maxwell-viscoelastic and hydrostatically pre-stressed Earth. The angular dependencies are treated by spherical harmonics. The radial dependencies are represented by finite-elements. This approach is typically referred to as the spectral–finite-elements approach. In accordance with Konrad et al. (2014), the Legendre cut-off degree has been fixed to $j = 256$ which corresponds to a

spatial resolution of ∼80 km. Cutting off the spectral response will decrease possible amplitudes of the solid-Earth response. However, the effect on bedrock slopes and RSL changes are expected to be negligible with $j = 256$ due to the low-pass filtering characteristic of the lithosphere and the relatively coarse horizontal resolution of the ISM.

2.2.1. Sea-level equation and surface loading

The deformation and the gravity changes are driven by an evolving surface load Σ, which is a composite of ice and ocean load: The surface load is determined from the ice thickness H while solving the sea-level equation (SLE; Farrell and Clark, 1976; Mitrovica and Milne, 2003), which presumes the coincidence of the ocean surface with an equipotential surface of the gravity field, the geoid, and the conservation of the global water budget. The change in RSL Δs, i.e. the effective change of the ocean-water column at each site, is the sum of the radial displacement of the Earth's surface, of the displacement of the reference equipotential surface, and of uniform sea-level variations. The latter is determined by the exchange of water between continental ice and the oceans and by the ocean-water redistribution due to the changes of ocean surface and ocean bottom. The SLE in the present SGVEM has been implemented by Hagedoorn et al. (2007). It includes changes in the rotational potential by the surface-mass redistribution, but in contrast to e.g. Mitrovica and Wahr (2011) neglects deformation due to changes in the rotation. de Boer et al. (2014) find that rotational feedbacks in coupled simulations are most important for the RSL response, but have a small effect on ice dynamics (10s of meters in ice thickness). At any given time, the load on the Earth's surface Σ is given by the ice thickness H and the RSL s:

$$\Sigma = \begin{cases} \rho\,H & \text{if } \rho\,H \geq \rho_{oc}\,s\,(\text{grounded ice/land}) \\ \rho_{oc}\,s & \text{else (floating ice/oceans)} \end{cases}. \qquad (6)$$

The Earth is assumed to be in hydrostatic equilibrium with the initial ice and ocean load Σ_0. Adhikari et al. (2014) found that the Earth's response to past ice changes in Antarctica will be outweighed by its response to future ice changes, judging from the response to the retreat in the SeaRISE experiments. This justifies the assumption of the Earth being in equilibrium with the initial ice load in our context.

An initial global bathymetry $\zeta = -s$ has to be specified. The commonly used ETOPO1 bathymetry (Amante and Eakins, 2009) is used here. In the Antarctic region (south of 60 °S), it is substituted by the BEDMAP2 data set (Fretwell et al., 2013), regridded as described in Section 2.3.

2.2.2. Earth structures

The radial density and shear modulus structures are taken from the Preliminary Earth Reference Model by Dziewonski and Anderson (1981). The SGVEM allows for consideration of heterogeneous viscosity structures. However, in this study, a radially symmetric 4-layer distribution of the viscosity is preferred over a three-dimensional structure for the sake of computational efficiency. Lateral heterogeneities may be taken into account in future studies. The radial distribution consists of a lower mantle (viscosity $\eta_{LM} = 2 \times 10^{22}$ Pa s), an upper mantle ($\eta_{UM} = 5 \times 10^{20}$ Pa s), a 200 km asthenospheric layer with the potential for low viscosity values between $\eta_A = 1 \times 10^{19}$ Pa s and 5×10^{20} Pa s, and an elastic lithosphere with practically infinite viscosity and thickness h_L varying between 40 km and 120 km (summarized in Fig. 2). The values for upper and lower mantle viscosity are consistent with Klemann et al. (2008) and lie between the values which were found optimal to explain geological or space-geodetic data all over Antarctica as reported by Whitehouse et al. (2012) ($\eta_{LM} = 1 \times 10^{22}$ Pa s; $\eta_{UM} = 1 \times 10^{21}$ Pa s) and Ivins et al. (2013) ($\eta_{LM} = 1.5 \times 10^{21}$ Pa s
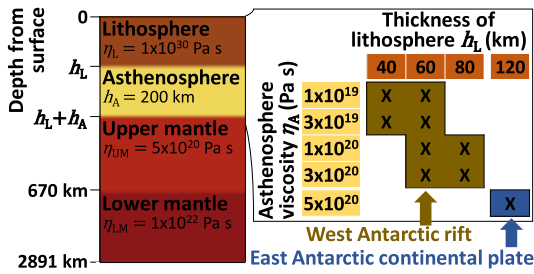
Fig. 2. Parameters of the prescribed viscoelastic Earth structures. The West Antarctic rift system is represented by the thickness of the elastic lithosphere h_L between 40 km and 80 km and an asthenosphere viscosity between 1×10^{19} Pa s and 3×10^{20} Pa s. The East Antarctic continental plate is modeled by a 120 km lithosphere and 5×10^{20} Pa s viscosity, used for both the asthenosphere and the upper mantle. The combinations considered here are marked by a cross in the matrix. The parameter distribution is radially symmetric (one-dimensional Earth model).

or 4×10^{21} Pa s; $\eta_{UM} = 2 \times 10^{20}$ Pa s). The highest values for asthenosphere viscosity (5×10^{20} Pa s) – reducing the Earth structure to three layers – and for lithospheric thickness (120 km) are chosen to roughly represent the cratonic setting of East Antarctica. The eight combinations of

$$\eta_A(\text{Pa s}) \in \{1 \times 10^{19},\ 3 \times 10^{19},\ 1 \times 10^{20},\ 3 \times 10^{20}\}$$

$$h_L\ (\text{km}) \in \{40,\ 60,\ 80\}$$

which are given in Fig. 2, are representations of the viscoelastic setting of the West Antarctic rifted system. The lower bound for the asthenospheric viscosity (1×10^{19} Pa s) is one to three orders of magnitude higher than values for other rifts reported by Ivins and Sammis (1995); hence, the associated short time scales of solid-Earth relaxation are probably not underestimated drastically, if at all. It is also in accordance with Kaufmann et al. (2005), who apply a viscosity gradient in the upper mantle (100 km to 450 km depth) from 1×10^{21} Pa s along the Transantarctic Mountains to $\sim 3 \times 10^{18}$ along the Amundsen Sea coast based on seismic tomography, and with van der Wal et al. (2015), who find values for the viscosity in the asthenosphere between 1×10^{18} Pa s and $\sim 1 \times 10^{21}$ Pa s for West Antarctica. The upper bound (3×10^{20} Pa s) yields a transition to the three-layered structure with $\eta_A = \eta_{UM} = 5 \times 10^{20}$ Pa s.

The parameter space spanned by these viscosity distributions is relatively narrow. In view of the computational cost for the simulations, we chose not to vary the thickness of the asthenospheric layer, or to introduce mid-range layers at the now relatively sharp transition from the low-viscous asthenosphere to the upper mantle (e.g. in the case of $\eta_A \leq 3 \times 10^{19}$ Pa s). Such features in the Earth structures would affect the wavelength spectrum of the Earth response to unloading as they would affect flow of mantle material. The slopes, the magnitudes and the characteristic times of the solid-Earth response, which all affect the stability of the ice sheet (Gomez et al., 2012; Adhikari et al., 2014), are consequently restricted to a certain part of the possible spectrum by our choice.

2.3. Coupling

The weak formulation of the solid-Earth dynamics in the SGVEM by Martinec (2000) implies an explicit time stepping for the viscoelastic deformation of the solid Earth, allowing a straight-forward coupling of the ISM and the SGVEM as the two models can advance in time synchronously. This is in contrast to other studies using coupled ice/Earth models, in which the normal-mode approach to viscoelastic deformation (Peltier, 1974) requires a spectral treatment of the temporal evolution and therefore a high computational cost for coupling to an ISM.

The two models exchange the fields of ice thickness and RSL after every coupling time interval Δt_C. Ice thickness changes, ΔH,

Table 1
Forcing scenarios for oceanic and atmospheric warming in Antarctica.

Scenario	ΔT_{oc}	ΔT_{at}
Weak	1.2 °C	2.4 °C
Medium	1.4 °C	2.8 °C
Strong	2.0 °C	4.0 °C

are updated in the SGVEM by the ISM output at a given coupling time t_i. The SGVEM then runs from $t_{i-1} = t_i - \Delta t_C$ to t_i while linearly interpolating the ice thickness between these two coupling times. Changes in RSL, Δs, at t_i are then updated in the ISM, which proceeds to t_{i+1}, while assuming zero changes in RSL between the two coupling times. The RSL changes are directly applied as changes of the bedrock topography. In accordance with Gomez et al. (2012) and Konrad et al. (2014), we choose $\Delta t_C = 50$ yr. This proved to be a sufficiently high resolution in idealized experiments (Konrad et al., 2014) and is much higher than in comparable model set-ups (Gomez et al., 2013; de Boer et al., 2014).

As the ISM operates on a regional Cartesian grid and the SLE solver of the SGVEM operates on a global Gauss–Legendre grid with 512×1024 grid nodes, the exchanged fields need to be regridded. This is done by bilinear interpolation, as in Gomez et al. (2013).

3. Perturbations of the initial steady state

3.1. Atmospheric and oceanic warming

The applied forcing consists of an instantaneous step-function for atmospheric and oceanic warming, by imposing constant positive values for ΔT_{at} and ΔT_{oc} at the start of the run (present-day, $t = 0$). Via Eqs. (2) and (3) and the PDD scheme, this leads to higher rates of snow precipitation, qualitatively consistent with findings by Frieler et al. (2015), melt water run-off on the ice-sheet surface, and higher rates of ice-shelf melting at the ice–ocean interface. The ocean-temperature increase ΔT_{oc} is applied to the Amundsen Sea Sector only (red outline in Fig. 1A), where the WAIS is most vulnerable due to incursions of warm circumpolar deep water (Thoma et al., 2008), and where oceanic warming in the present and in the future is also most likely (Bindschadler et al., 2013). Consequently, the mass loss in the simulations occurs mainly in areas where the AIS is observed to be losing mass today.

Three different forcing scenarios are considered (Table 1): a weak forcing with $\Delta T_{oc} = 1.2\,°C / \Delta T_{at} = 2.4\,°C$, a medium forcing with $\Delta T_{oc} = 1.4\,°C / \Delta T_{at} = 2.8\,°C$, and a strong forcing with $\Delta T_{oc} = 2.0\,°C / \Delta T_{at} = 4.0\,°C$. Ligtenberg et al. (2013) report an increase of the 2 m air temperature over Antarctica by 2.4–5.3 °C until 2200 AD obtained from regional climate modeling, depending on the respective IPCC AR5 scenario, which approximately corresponds to the span of the chosen values for ΔT_{at}. The related change of surface mass balance in this study might differ from the results of Ligtenberg et al. (2013), however, as it is simply parameterized by Eq. (2) and the PDD scheme. Timmermann and Hellmer (2013) report $\sim 1\,°C$ of ocean warming in the Amundsen Sea area from 2010 to 2200 under several IPCC AR5 scenarios. We considered a stronger ocean temperature perturbation in order to force WAIS collapse (Section 4.1.1). However, the actual sub-shelf melt rates from our parametrized approach and from Timmermann and Hellmer (2013) cannot be directly compared.

A warming of the ocean waters below the Ross Ice Shelf should enhance the possibility of a future WAIS collapse, and a more realistic assessment of the WAIS collapse would need a respective consideration. Also, a more realistic transition to warmer climate conditions could be applied instead of an instantaneous atmo-
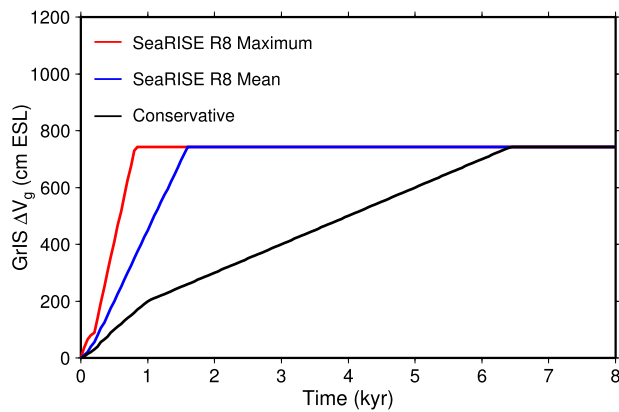
Fig. 3. Time evolution of ice loss according to three deglaciation scenarios for the GrIS. The two fast deglaciation scenarios (red and blue) are based on the SeaRISE R8 experiments (Bindschadler et al., 2013). The black curve illustrates a more conservative GrIS deglaciation scenario. The maximum GrIS contribution to sea-level rise is ∼7.4 m ESL. Note that the complete GrIS melting in the two fast scenarios occurs earlier than in the most extreme case by Robinson et al. (2012), see main text. (For interpretation of the references to color in this figure legend, the reader is referred to the web version of this article.)

spheric and oceanic forcing. The impact, however, on the time scales investigated in this study (20 kyr) is expected to be minor.

3.2. Sea-level rise from Greenland Ice Sheet and glacier melting

The GrIS stores $\sim 2.96 \times 10^{6}$ km^3 of ice or $\sim$7.4 m of equivalent sea level (ESL) (Bamber et al., 2013). Three deglaciation scenarios for the present-day GrIS have been created (Supplement S.2) for the purpose of forcing the AIS by additional sea-level rise from Greenland melt water. The rates at which the GrIS discharges ice into the oceans are based in part on the SeaRISE R8 experiment (Bindschadler et al., 2013) in which maximum and mean ESL contributions at $t = 100$ yr, 200 yr and 500 yr are found. These have been extrapolated until the GrIS has completely vanished. In the case of the maximum contributions (red curve in Fig. 3), the entire GrIS is melted within the first 850 yr. The mean scenario (blue) takes 1600 yr. A more conservative scenario is defined which corresponds to a complete melting of the GrIS after 6450 yr (black curve). These values correspond to average rates of sea-level rise of 8.7 mm/yr, 4.6 mm/yr, or 1.1 mm/yr, respectively. Complete melting of the GrIS within 2 kyr to 10 kyr in a warming climate has been found to be plausible by Robinson et al. (2012), which indicates that the two SeaRISE-based scenarios are likely to overestimate the timing for total GrIS decay due to simple extrapolation. In general, the scenarios are simplistic and do not take into account interactions with changing climate on millennial time scales.

Additionally, a global glacier ice component to sea-level rise has been constructed, contributing another $\sim$0.4 m ESL (Supplement S.2). Glaciers in Greenland and Antarctica are excluded as they are included either in the description above (Greenland) or in the explicit ice dynamical modeling (Antarctica). The glacier melting represents a linear decrease of glacier ice thickness towards zero within the first 2000 years.

In the experiments, the above prescription of atmospheric and oceanic warming is combined with the different GrIS deglaciation scenarios and the glacier melting. It is important to note that neither the mass loss of the GrIS nor that of the other glaciated regions is explicitly modeled in these experiments, but their effects are prescribed as an additional far-field sea-level forcing of the AIS by summing up the respective global ice-thickness fields when handing the AIS ice thickness from the ISM to the SGVEM
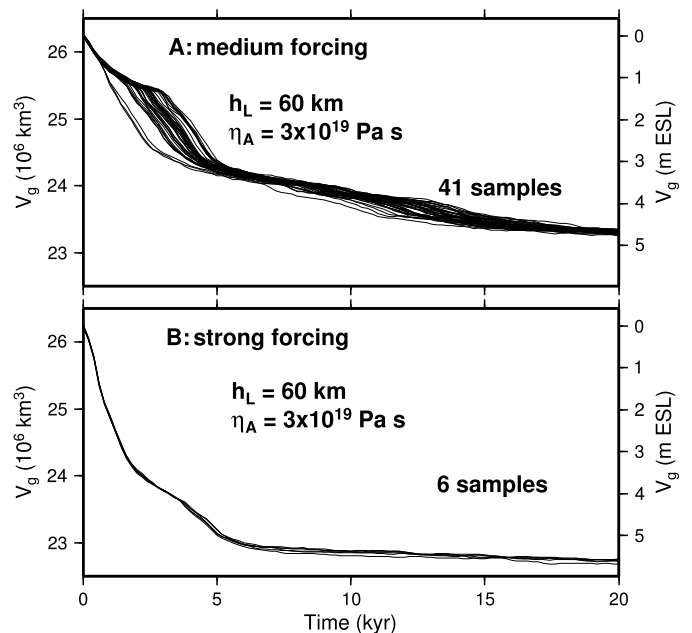

Fig. 4. Simulated temporal evolution of Antarctic ice volume (V_g) for selected ensembles. The ensembles in A and B are defined by the forcing strength and the Earth structure. A: medium atmospheric and oceanic forcing; no GrIS or glacier melting; $h_L = 60$ km/$\eta_A = 3 \times 10^{19}$ Pa s Earth structure. B: strong atmospheric and oceanic forcing; no GrIS or glacier melting; $h_L = 60$ km/$\eta_A = 3 \times 10^{19}$ Pa s Earth structure. The spread of the 41 samples in A is notable, whereas the six samples in B show a more tightly grouped evolution. The right ordinate gives an estimate of equivalent sea level, computed as $\rho \, \Delta V_g^{\mathrm{af}}/\rho_{\mathrm{oc}}/A_{\mathrm{oc}}$ with ocean area A_{oc} fixed to 3.619×10^8 km^2 and the change in grounded ice volume above flotation ΔV_g^{af}. Note that in the considered volume range for the AIS, ΔV_g^{af} is only an approximately linear function of V_g.

(Section 2.3). By that, the SLE is solved consistently with this prescribed additional ice loss.

4. Results

4.1. Dependence of the WAIS stability on the solid-Earth structure

The results discussed in Section 4.1 are obtained without additional sea-level forcing from the GrIS or the glacier melting, but solely by increasing atmospheric and oceanic temperatures according to the classifications above (weak, medium, strong; Table 1).

Precursor studies showed a random component in the retreat behavior for moderate GL retreat rates: The timing of the collapse is sensitive to the initial state and to the numerical precision of the coupling procedure. Consequently, the timing of the potential WAIS collapse cannot be determined by single simulations but rather by ensembles with slightly different initial states (Supplement S.3). Note that the numerical precision does not affect the quality of the results discussed below as they are obtained from the ensembles. The large spread in the scenario with medium forcing (shown for example for one Earth structure in Fig. 4A) required a relatively large ensemble of 41 samples. The much smaller spread in the case of the strong forcing (Fig. 4B) allows us to work with smaller ensembles of only six samples. Mean temporal evolutions are derived from these ensembles for further discussion in this section. WAIS collapse does not occur in the weakly forced scenarios (see below). Therefore, the results do not spread and the presented results are based on one single simulation. Note that the WAIS is either always stable or always collapsed for all members of one ensemble (i.e. for fixed forcing strength and Earth structure but different initial states), so that the stability can in principle be inferred from one representative sample.
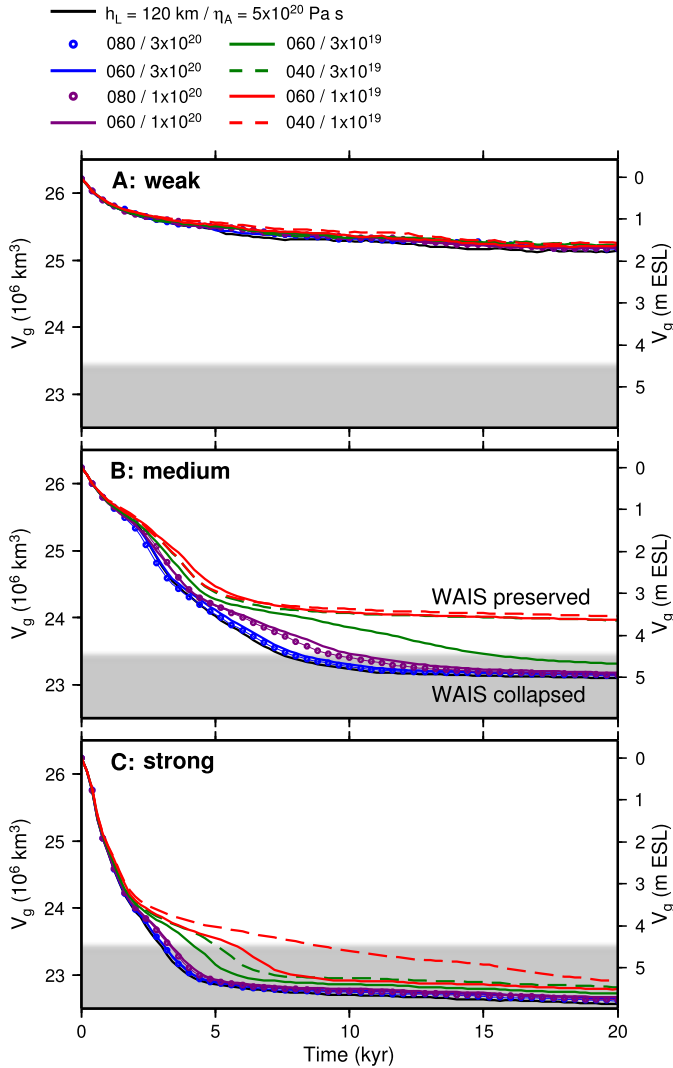
Fig. 5. Time-evolution curves of Antarctic grounded ice for the simulations with different Earth structures. A: weak forcing; B: medium forcing; C: strong forcing (no GrIS or glacier melting here). The grey shading indicates the volume at which the break-through from the Amundsen Sea to the Ross Ice Shelf occurs ($V_{g,bt} \approx 23.5 \times 10^6$ km^3, see main text). B and C show the respective ensemble mean curves.

4.1.1. Evolution of grounded ice

Fig. 5 shows the temporal evolution of grounded ice volume in Antarctica for the three forcing scenarios and the nine Earth structures. In the cases of the medium forcing (B) and the strong forcing (C), the curves show the mean evolution of the respective ensembles.

In all simulations, the oceanic and atmospheric warming leads to loss of grounded ice, specifically in the WAIS. However, a complete WAIS collapse does not necessarily occur in all simulations. In the context of this study, the WAIS is considered collapsed if there is an open-ocean or ice-shelf connection from the Amundsen Sea to the Ross Ice Shelf and to the Filchner-Ronne Ice Shelf. This is found to occur if the grounded ice volume drops below $V_{g,bt} \approx 23.5 \times 10^6$ km^3. The loss of grounded ice ($\sim 3 \times 10^6$ km^3 or ~ 4.5 m ESL) does not only originate in West Antarctica, but also in East Antarctica (Pollard et al., 2015) as the atmospheric warming is applied to the entire AIS and leads to ablation and thus retreat in coastal areas of the EAIS. However, as verified at least once per ensemble, the above coincidence of $V_{g,bt}$ with the break-through holds for all our simulations.

Fig. 5 clearly shows that grounded ice loss follows one of two pathways; WAIS collapsed ($V_g < V_{g,bt}$ after 20 kyr) or WAIS preserved ($V_g > V_{g,bt}$). In the explored range of climate forcings, the weak warming leads to preservation of the WAIS, whereas the strong warming leads to its collapse. In both cases, the pathway which the ice/Earth system follows is independent of the Earth structure, even though the timing is not (Section 4.1.3).

For the medium forcing, however, the Earth structure governs whether the WAIS is finally preserved or collapsed: Simulations with weak Earth structures, i.e. $h_L = 40$ km$/\eta_A = 3 \times 10^{19}$ Pa s (dashed green line in Fig. 5B), $h_L = 60$ km$/\eta_A = 1 \times 10^{19}$ Pa s (solid red), and $h_L = 40$ km$/\eta_A = 1 \times 10^{19}$ Pa s (dashed red), lead to a final state with preserved WAIS. The combination of $h_L = 60$ km and $\eta_A = 3 \times 10^{19}$ Pa s (solid green) yields a transitional behavior with a slow collapse. For this case, as well as for stiffer Earth structures, the stabilization by RSL fall is not sufficient to preserve the WAIS (Section 4.1.2). Under the strong forcing, $h_L = 40$ km$/\eta_A = 1 \times 10^{19}$ Pa s considerably delays the disintegration and yields ongoing ice loss even after 20 kyrs. The final ($t = 20$ kyr) difference in grounded ice volume between the AIS with the WAIS preserved and the WAIS collapsed under the medium forcing is $\sim 0.9 \times 10^6$ km^3 or an additional equivalent sea-level rise by 1.4 m for the collapsed WAIS.

4.1.2. Stabilization by rapid RSL fall

The stabilization of the WAIS by RSL fall is now studied on the basis of particular examples, by comparing the situations before and after the potential collapse for $h_L = 60$ km and $\eta_A = 1 \times 10^{19}$ Pa s or 3×10^{19} Pa s in the mediumly forced scenario. The WAIS on the $\eta_A = 3 \times 10^{19}$ Pa s Earth finally collapses (green solid line in Fig. 5B), whereas it is preserved on the $\eta_A = 1 \times 10^{19}$ Pa s Earth (red solid line). For a better comparison and to avoid misinterpreting the effect caused by the random behavior, the common value for V_g is preferred over the same time for discussing the situation before the collapse. We choose the arbitrary value of $V_{g,1} = 24.34 \times 10^6$ km^3, which is close to the later steady-state volume in the case of the stable WAIS. The WAIS has not collapsed yet when the AIS reaches this value during its retreat ($V_{g,1} > V_{g,bt}$). The times at which the two simulations reach this value differ by 1.6 kyr. This is due to (1) the random timing of the collapse which made the sampling necessary in the first place[2] and (2) the stabilizing effects of the weaker asthenosphere ($\eta_A = 1 \times 10^{19}$ Pa s).

Fig. 6 shows the changes of RSL since $t = 0$, before the potential collapse ($V_g = V_{g,1}$, A: $\eta_A = 1 \times 10^{19}$ Pa s at $t = 6.6$ kyr; B: $\eta_A = 3 \times 10^{19}$ Pa s at $t = 5$ kyr), and after 20 kyr (D: $\eta_A = 1 \times 10^{19}$ Pa s; E: $\eta_A = 3 \times 10^{19}$ Pa s), as well as the respective differences between the simulations based on the two Earth structures at the earlier time (C). When $V_g = V_{g,1}$ (A and B), the grounded ice loss is similar for simulations with different asthenosphere viscosities as indicated by the GL position. Most pronounced deviations occur along Siple Coast, in the hinterland of the Ross Ice Shelf, where the GL differs most. In both cases, there is already a small open-ocean (or ice-shelf) connection from the Amundsen Sea to the Filchner-Ronne Ice Shelf. In the case of $\eta_A = 1 \times 10^{19}$ Pa s, however, the ocean is shallower, due to (1) the faster asthenospheric response (lower viscosity) and (2) the longer time for adjustment (6.6 kyr vs. 5 kyr). The decrease in ocean depth caused mainly by the uplift is strong enough to cease GL retreat and prevent further collapse of the WAIS; the GL remains close to its position at 6.6 kyr in the ongoing evolution for this viscosity structure.

In contrast, the WAIS has collapsed in the case of $\eta_A = 3 \times 10^{19}$ Pa s after 20 kyrs; all grounded and floating ice is lost in the region between the Ross Sea and the Amundsen Coast where ice

---

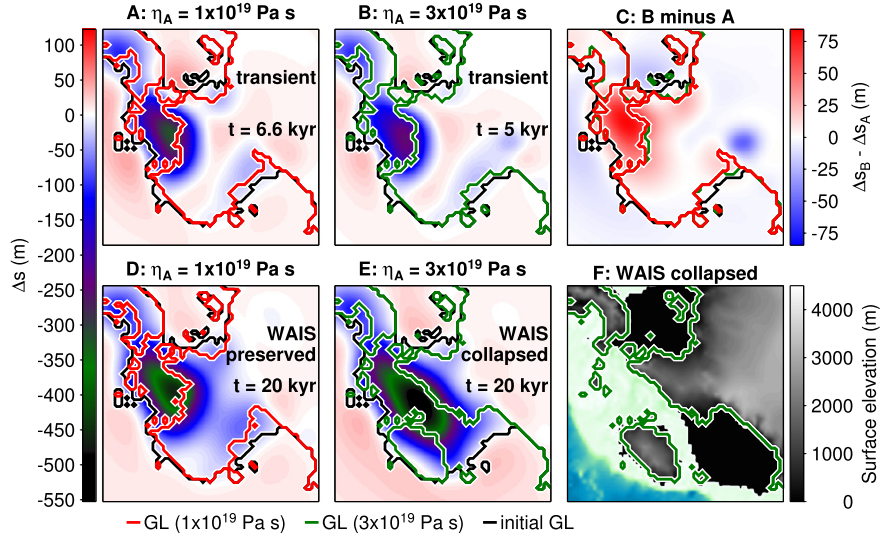[2] The illustrated fields are from one ensemble member each.

Fig. 6. Change of RSL, Δs, since $t = 0$ over West and central Antarctica (outline in Fig. 1A). A: Medium forcing scenario with the $h_L = 60$ km$/\eta_A = 1 \times 10^{19}$ Pa s Earth structure at $t = 6.6$ kyr. B: Medium forcing scenario with the $h_L = 60$ km$/\eta_A = 3 \times 10^{19}$ Pa s Earth structure at $t = 5$ kyr. C: Difference between the Δs-fields in A and B. The colors of the GLs refer to the respective colors for GLs in A and B. D: The same as A at $t = 20$ kyr. E: The same as B at $t = 20$ kyr. F: The final state in E (WAIS collapsed) in the color-coding of Fig. 1A showing ice-sheet surface elevation. Negative values in A, B, D, and E indicate bedrock uplift or decrease of ocean depth, respectively. Positive values in C indicate a higher uplift/shallower ocean for $\eta_A = 1 \times 10^{19}$ Pa s which stabilizes the ice sheet. (For interpretation of the references to color in this figure legend, the reader is referred to the web version of this article.)
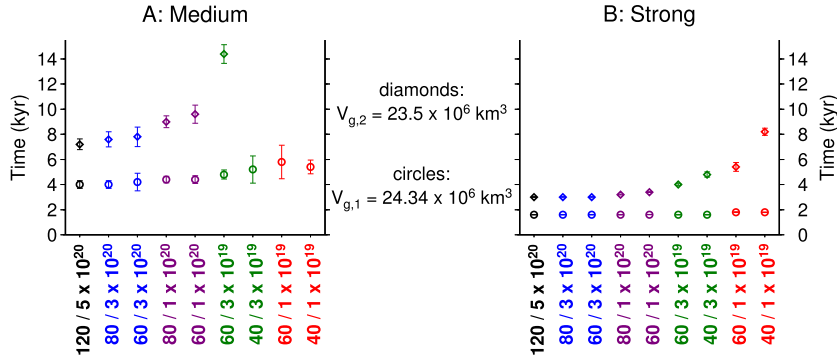

Fig. 7. Time to reach the threshold values of grounded ice volume of $V_{g,1}$ (before potential collapse; white background) and $V_{g,2}$ (break-through; grey shading) for all Earth structures (h_L/η_A in km/Pa s). A: medium forcing; B: strong forcing. Error bars represent the ensemble standard deviation. Note that the WAIS does not collapse for the three weakest Earth structures for the medium forcing, and so the values for $V_{g,2}$ are not defined in these cases.

was previously grounded below sea level. At this stage, the RSL is considerably lower than before the collapse due to uplift associated with the grounded ice retreat and unloading of the Earth.

4.1.3. Delay of the WAIS collapse by a weak Earth structure

Fig. 5B and C indicate differences in the timing of the collapse for different Earth structures for the medium and strong forcings, respectively, which will now be investigated further. To compare the time evolutions of grounded ice, we define two threshold values; $V_{g,1} = 24.34 \times 10^6$ km^3 corresponds to the state of the AIS well in advance of a potential collapse as shown in Fig. 6A and B, whereas $V_{g,2} = 23.5 \times 10^6$ km$^3 \approx V_{g,bt}$ represents the situation of a break-through from the Amundsen Sea to the Ross Ice Shelf. The points in time, at which the thresholds $V_{g,1}$ and $V_{g,2}$ are passed, are shown in Fig. 7 based on the temporal evolution of ensemble means shown in Fig. 5.

The time to reach the earlier state ($V_{g,1}$) exhibits much less spread for different Earth structures than the time to reach the break-through ($V_{g,2}$), particularly in the case of the strong forcing. The break-through time increases for weaker Earth structures due to the slower decay of the WAIS. In the mediumly forced scenario, the value $V_{g,2} = 23.5 \times 10^6$ km^3 associated with the WAIS collapse

is reached 7 to 14 kyr after the onset of the forcing. Under the strong forcing, this value is reached after 3 to 8 kyr.

In the following, the temporal difference to reach a given volume $V_{g,k}$ ($k = 1, 2$) is evaluated for two Earth structures i and j according to:

$$\Delta t_{d,ijk} = t_i(V_{g,k}) - t_j(V_{g,k}) \, , \tag{7}$$

where the differences are considered significant, if

$$\Delta t_{d,ijk} > \sqrt{\left(\Delta t_{std,i}(V_{g,k})\right)^2 + \left(\Delta t_{std,j}(V_{g,k})\right)^2} \tag{8}$$

with Δt_{std} being the ensemble standard deviation. Only differences which are significant in this sense are discussed. A per-Earth structure comparison is given in Supplement S.5.

$V_{g,1} = 24.34 \times 10^6$ km^3 is reached during WAIS retreat in the scenario with medium forcing between 0.7 and 1.8 kyr later in the case of an asthenosphere viscosity $\eta_A < 3 \times 10^{20}$ Pa s when compared to the $\eta_A \geq 3 \times 10^{20}$ Pa s results. Differences in the lithospheric thickness do not lead to significant delay for any of the values for asthenosphere viscosity. In the strongly forced scenario, $V_{g,1} = 24.34 \times 10^6$ km^3 is reached almost at the same time in all simulations with a delay of 0.2 kyr or less.

The second illustrated value $V_{g,2} = 23.5 \times 10^6$ km^3 (break-through from the Amundsen Sea to the Ross Ice Shelf; see above)
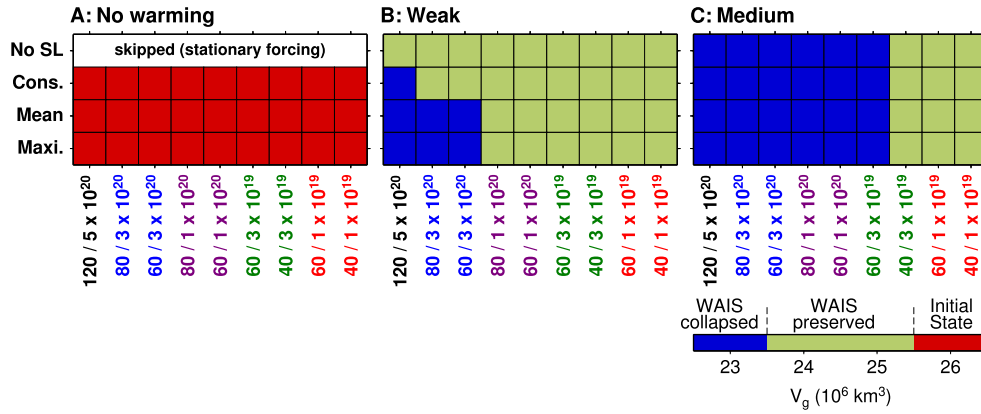
Fig. 8. Final AIS grounded ice volume after 20 kyr for different combinations of sea-level rise and atmospheric/oceanic forcing. The top rows in B and C correspond to the ensemble results in Fig. 5B and C. All remaining values are from single simulations instead of ensembles. The labels of the color scale are in accordance with Section 4.1. No SL: No GrIS deglaciation and no glacier melting; Cons.: Conservative GrIS deglaciation scenario; Mean: Mean R8 deglaciation scenario; Maxi.: Maximum R8 deglaciation scenario. The GrIS melting scenarios are always accompanied by complete glacier melting within 2000 yr (see Section 3.2 for details). Here, the deglaciation of the GrIS is always complete in contrast to Fig. 9. (For interpretation of the references to color in this figure legend, the reader is referred to the web version of this article.)
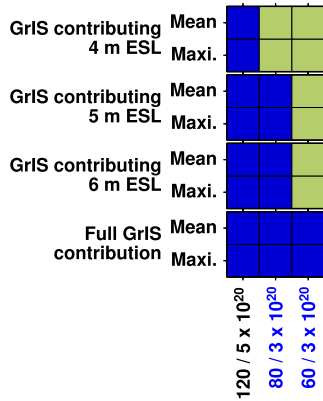

Fig. 9. Same as Fig. 8B (weak atmospheric/oceanic forcing), but with variable absolute contribution of the GrIS to sea-level rise, and without contributions from glacier melting. Only the sensitive stiffer Earth structures are shown. The color scale is the same as in Fig. 8. (For interpretation of the references to color in this figure legend, the reader is referred to the web version of this article.)

is not reached under the medium forcing in the simulations featuring the three weakest Earth structures. The collapse in the $\eta_A = 1 \times 10^{20}$ Pa s simulations is delayed by 1.1 to 2.4 kyr when compared to a stiffer asthenosphere. The gradual decay of the WAIS in the case of the $h_L = 60$ km/$\eta_A = 3 \times 10^{19}$ Pa s Earth (Section 4.1.1, Fig. 5B) leads to a delay of the collapse of more than 4.7 kyr. Again, differences in lithospheric thickness alone do not delay the AIS reaching the respective volume threshold significantly, except for $\eta_A = 3 \times 10^{19}$ Pa s; then, the lithospheric thickness influences the stability itself. The strong forcing, which causes the WAIS collapse for all applied Earth structures, yields temporal delays that are almost all significant. The delay between $\eta_A = 3 \times 10^{20}$ Pa s and $\eta_A = 1 \times 10^{20}$ Pa s becomes very small (≤ 0.5 kyr), whereas a weaker asthenosphere $\eta_A \leq 3 \times 10^{19}$ Pa s causes a delay between 0.8 and 5.2 kyr. Within this range of low viscosities, for which the delay is up to 4 kyr, the values for η_A are very important for the exact timing of the WAIS collapse. Differences in the lithospheric thickness also provide significant and rather long delays of the collapse of 0.8 kyr ($h_L = 40$ km vs. $h_L = 60$ km in the case of $\eta_A = 3 \times 10^{19}$ Pa s) or 2.6 kyr ($\eta_A = 1 \times 10^{19}$ Pa s).

4.2. Impact of additional sea-level rise from GrIS and glacier melting

Up to this point, all results have been obtained without considering future sea-level rise caused by GrIS or glacier melting.

Additional experiments are now evaluated, for which the weak or the medium atmospheric/oceanic forcing is combined with additional sea-level forcing caused by the decay of the GrIS at various rates and the linear glacier melting within 2000 yr as described in Section 3.2. The strong atmospheric/oceanic forcing is omitted here because the WAIS collapses without further forcing. We aim here to show only the general impact of far-field sea-level rise, so that single simulations instead of ensembles are considered.

The results are summarized in Fig. 8. Frame A shows the results in the case of sea-level rise but no atmospheric or oceanic warming. It is obvious that the steady-state AIS is not responding to the sea-level rise – no matter at which rate it occurs. Frame C (medium atmospheric and oceanic warming) shows no differences with the varying sea-level forcing: In each frame, the WAIS is only stable in the cases of the three weakest Earth structures, as discussed in Section 4.1.1.

However, when applying the weak warming perturbation, which leaves the WAIS stable for all Earth structures without additionally forced sea-level rise, the sea-level rise has a significant impact: The WAIS collapses in the presence of the strongest (East Antarctic) Earth structure ($h_L = 120$ km/$\eta_A = 5 \times 10^{20}$ Pa s), independently of the rates at which the GrIS decays. In contrast, for Earth structures with asthenosphere viscosities $\eta_A \leq 1 \times 10^{20}$ Pa s, the WAIS is always preserved, likewise independently of the applied decay rate. For $\eta_A = 3 \times 10^{20}$, the WAIS collapses if the rate of the GrIS decay is sufficiently high (mean or maximum R8 scenarios), but is preserved if the GrIS decays at the conservative rates.

In order to test the impact of the magnitude of sea-level rise, further experiments with the weak atmospheric and oceanic forcing have been carried out, neglecting the sea-level contribution of the glaciers and prescribing lower maximum contributions of the GrIS deglaciation (4 m ESL, 5 m ESL, 6 m ESL). Fig. 9 shows the respective results for the range of stiffer Earth structures, for which the WAIS collapse depends on the GrIS decay rate according to the analysis above. The WAIS collapses without forcing from the glacier melting if the GrIS decays completely, indicating that the small contribution of 0.4 m ESL from the glaciers is negligible. A smaller contribution of the GrIS to sea-level rise, however, affects only the WAIS on the East Antarctic solid-Earth representation and the stiffest of the West Antarctic rheologies ($h_L = 80$ km, $\eta_A = 3 \times 10^{20}$ Pa s). The RSL fall corresponding to the third considered Earth structure, which differs from the latter only by the thinner lithosphere (60 km), compensates the additional sea-level rise. If the GrIS contribution drops below 5 m ESL,

the $h_L = 80$ km$/\eta_A = 3 \times 10^{20}$ Pa s Earth also provides stability to the WAIS, whereas the slow and smaller RSL fall related to the East Antarctic rheology still yields the collapse.

5. Discussion

The ice loss in the first $\sim$2 kyr of the experiments is governed by the strength of the atmospheric and oceanic forcing (Fig. 5); no differences arise from the different Earth structures in this first stage. If the forcing is sufficiently weak (i.e. in the weakly forced scenario), this independence from the Earth structure extends over the whole time span of 20 kyr, because relatively little GL retreat is involved. A stronger forcing leads to substantial GL retreat in the WAIS, with considerable deviations in grounded ice loss arising for different Earth structures after only 2 kyr (Fig. 5B, C). In the longer-term evolution, the solid-Earth response to the GL retreat becomes crucial, as it governs whether the WAIS collapse is prevented by fast relaxation of the Earth and an associated RSL drop. The (in-)stability is directly related to the magnitude of the RSL response to the ice retreat in the Amundsen Sea embayment before the GL retreat reaches a critical extent (Fig. 6C). The potential of the solid-Earth response to prevent WAIS collapse depends on the interplay between the viscosity structure and the forcing strength; the stronger the forcing, the weaker the Earth is required to produce WAIS stability. After exceeding a certain threshold of climate warming, even the weakest solid-Earth layering used here cannot prevent the WAIS from collapsing. Nevertheless, the delay of the WAIS collapse imposed by a fast solid-Earth response can easily be greater than 4 kyr (Fig. 7), which is significant in comparison to the time that it takes the WAIS to collapse (3 kyr to 14 kyr).

The lithospheric thickness leads to significant differences in the decay of the WAIS in the presence of a low asthenosphere viscosity. A thinner lithosphere produces WAIS stability where a thicker does not ($\eta_A = 3 \times 10^{19}$ Pa s under the medium forcing; Fig. 5B), or it delays the collapse by 0.8 kyr ($\eta_A = 3 \times 10^{19}$ Pa s under the strong forcing; Fig. 5C) or 2.6 kyr ($\eta_A = 1 \times 10^{19}$ Pa s under the strong forcing).

We emphasize that these results are also affected by the thickness of the asthenospheric layer (200 km) or the four-layer characteristic in general. In simulations where the WAIS would otherwise be preserved (e.g. $h_L = 40$ km$/\eta_A = 3 \times 10^{19}$ Pa s/medium forcing), a thinner asthenosphere can lead to too small a response over the limited time span for stabilization, causing the WAIS to collapse. On the other hand, a thicker asthenosphere or a more gradual transition to the value of upper mantle viscosity may avoid collapse and preserve the WAIS (e.g. for $h_L = 60$ km$/\eta_A = 3 \times 10^{19}$ Pa s/medium forcing). The timing of the ice loss as discussed in Section 4.1.3 is also affected by a different layering.

The potential sea-level rise from the GrIS additionally destabilizes the WAIS for stiff Earth structures ($\eta_A \geq 3 \times 10^{20}$ Pa s; Figs. 8, 9), but mainly for the two unrealistically fast deglaciation scenarios. This indicates that sea-level rise in our experiments is a driver of WAIS collapse only if it occurs at high rates above a certain threshold and if it is accompanied by climate warming. Depending on the magnitude of the forced sea-level rise, the lithospheric thickness may also play an important role for the WAIS stability for the relatively stiff Earth structure with $\eta_A = 3 \times 10^{20}$ Pa s. With weaker Earth structures, GrIS melting does not induce WAIS collapse, because the more rapid uplift of a weaker Earth produces shallower oceans in West Antarctica early enough, even in the case of a fast GrIS decay.

The strength of the atmospheric and oceanic forcing remains the primary constraining factor which governs the stability and collapse of the WAIS. An increased sensitivity of the ice sheet to this forcing as given by the hydro-fracturing and cliff-failure mechanisms proposed by Pollard et al. (2015), which have not been

taken into account here, would probably decrease the potential of the solid-Earth deformation to stabilize the WAIS. However, for situations in which the collapse and preservation of the WAIS are possible, the viscoelastic response determines the pathway which the ice sheet will follow, and thus has to be modeled accurately.

We have applied one-dimensional radial Earth structures for the whole of Antarctica, but the ice loss occurs mainly in the hinterland of the Amundsen Sea coast and Marie Byrd Land (Fig. 6). The question that remains is which solid-Earth structure is most appropriate for modeling the viscoelastic response in this region. Earlier studies on Antarctic GIA have mostly applied a laterally uniform one-dimensional Earth structure representing the whole of Antarctica (Whitehouse et al., 2012; Ivins et al., 2013), or have focused on regions which are relatively far apart and tectonically separated from the West Antarctic rift (Nield et al., 2012). To our knowledge there are no studies on regional scales for the Amundsen Sea coast in which viscoelastic parameters are adjusted explicitly to GIA-related observations such as long-term trends in GPS-detected surface uplift. Groh et al. (2012) suggest lower viscosities compared to standard models for Antarctica in the region of interest to explain the observed high rates of viscoelastic vertical motion along the Amundsen Sea coast, but give no specific values. Based on this suggestion, the lower range of asthenosphere viscosities in the present study seems plausible.

The Earth response in East Antarctica in the present experiments is likely to be overestimated by the applied West Antarctic Earth structures, which would not be the case if lateral variations of the Earth structures were accounted for. This will be carried out in future studies. However, we think that the effect of biased EAIS dynamics on WAIS dynamics due to too fast vertical bedrock motion in East Antarctica is negligible, as the Transantarctic Mountains serve as a natural barrier for ice flow (Paulsen and Wilson, 2004). Additionally, the ice loss and the forced RSL changes are much smaller in the case of the EAIS compared to the WAIS retreat, so that these do not influence our results for the WAIS. Therefore, we assume that our findings on WAIS collapse or stability are not biased by the choice of one-dimensional Earth structures. The most complete approach would be to apply an observationally based three-dimensional viscosity field (van der Wal et al., 2015).

6. Conclusions

We have shown that solid-Earth deformation exerts an important control on the possibility of future WAIS collapse and its timing on the time scale of several 1000s of years, i.e. for time intervals covering an interglacial, for simplistic climate warming and Greenland melt scenarios and a limited, but reasonable range of Earth parameters. During the first 2–3 kyr of our experiments, the ice loss is mainly governed by the intensity of atmospheric and oceanic warming, and it is only later that the millennial-scale interaction of the ice sheet with the solid Earth becomes important. In the presence of a weak Earth structure, the bedrock will rebound rapidly. The associated local decrease in ocean depth may stabilize WAIS retreat, if the climatic warming does not exceed a certain threshold. For a more intense climate forcing, for which the collapse of the WAIS cannot be prevented by the decrease in ocean depth in our simulations, a weak Earth structure still delays the disintegration of the WAIS. This indicates that a comprehensive modeling study of the long-term behavior of the WAIS requires a thoughtfully constructed representation of the solid Earth. Substantial sea-level rise caused by melt water from the GrIS may induce WAIS collapse for stiff Earth structures in cases when the atmospheric and oceanic warming in Antarctica is too weak to force WAIS collapse alone. Weaker Earth structures easily compensate the additional forcing exerted by the GrIS deglaciation. In

summary, the stabilization by solid-Earth deformation investigated here is of secondary importance compared to the climate forcing; however, for conditions which do not emphatically favor stability or instability, the viscoelastic deformation governs the pathway of WAIS collapse through an interglacial.

Acknowledgements

Appendix A. Variables and parameters

Table 2
Parameters and variables used in this manuscript. Values of fixed parameters are specified in the second column.

A_{oc}		ocean area
$\dot{b}$		accumulation rate
$\dot{b}_{PD}$		present-day values of accumulation rate
$\dot{b}_s$		sub-shelf melt rate
c_p	4218 J/kg/K	specific heat of ocean water
h_L		lithosphere thickness
H		ice thickness
K_B	3	scaling factor
K_T	15.77 m/yr/K	transfer factor
L	335×10^3 J/kg	latent heat of fusion
s		relative sea level
s_{oc}	34.5 PSU	ocean water salinity
S		ice sheet surface elevation
S_{PD}		present-day observations of ice sheet surface elevation
t		time
T		ice surface temperature
T_f		freezing point temperature
T_{oc}		ocean temperature
$T_{oc,0}$		initial ocean temperature
T_{PD}		present-day observations of ice surface temperature
V_g		grounded ice volume
z		depth below sea level
γ	0.008 °C/m	lapse rate
Δt_C	50 yr	coupling interval
ΔT_{at}		atmospheric temperature offset
ΔT_{oc}		oceanic temperature offset
V_g^{af}		volume above flotation
η_A		asthenosphere viscosity
η_{LM}	2×10^{22} Pa s	lower mantle viscosity
η_{UM}	5×10^{20} Pa s	upper mantle viscosity
ρ	910 kg/m^3	density of ice
ρ_{oc}	1020 kg/m^3	density of ocean water
Σ		surface load
Σ_0		surface load at $t = 0$
ζ		bathymetry

Appendix B. Supplementary material

Supplementary material related to this article can be found online at http://dx.doi.org/10.1016/j.epsl.2015.10.008.

References

Accardo, N.J., Wiens, D.A., Hernandez, S., Aster, R.C., Nyblade, A., Huerta, A., Anandakrishnan, S., Wilson, T., Heeszel, D.S., Dalziel, I.W.D., 2014. Upper mantle seismic anisotropy beneath the West Antarctic Rift System and surrounding region from shear wave splitting analysis. Geophys. J. Int. http://dx.doi.org/10.1093/gji/ggu117.

Adhikari, S., Ivins, E.R., Larour, E., Seroussi, H., Morlighem, M., Nowicki, S., 2014. Future Antarctic bed topography and its implications for ice sheet dynamics. Solid Earth 5 (1), 569–584. http://dx.doi.org/10.5194/se-5-569-2014.

Amante, C., Eakins, B.W., 2009. Etopo1 1 arc-minute global relief model: procedures, data sources and analysis. NOAA Tech. Memorandum NESDIS NGDC 24. http://dx.doi.org/10.7289/V5C8276M.

Augustin, L., Barbante, C., Barnes, P.R.F., Barnola, J.M., Bigler, M., Castellano, E., Cattani, O., Chappellaz, J., Dahl-Jensen, D., Delmonte, B., Dreyfus, G., Durand, G., Falourd, S., Fischer, H., Flückiger, J., Hansson, M.E., Huybrechts, P., Jugie, G., Johnsen, S.J., Jouzel, J., Kaufmann, P., Kipfstuhl, J., Lambert, F., Lipenkov, V.Y., Littot, G.C., Longinelli, A., Lorrain, R., Maggi, V., Masson-Delmotte, V., Miller, H., Mulvaney, R., Oerlemans, J., Oerter, H., Orombelli, G., Parrenin, F., Peel, D.A., Petit, J.-R., Raynaud, D., Ritz, C., Ruth, U., Schwander, J., Siegenthaler, U., Souchez, R., Stauffer, B., Steffensen, J.P., Stenni, B., Stocker, T.F., Tabacco, I.E., Udisti, R., van de Wal, R.S.W., van den Broeke, M., Weiss, J., Wilhelms, F., Winther, J.-G., Wolff, E.W., Zucchelli, M., 2004. Eight glacial cycles from an Antarctic ice core. Nature 429 (6992), 623–628. http://dx.doi.org/10.1038/nature02599.

Bamber, J.L., Griggs, J.A., Hurkmans, R.T.W.L., Dowdeswell, J.A., Gogineni, S.P., Howat, I., Mouginot, J., Paden, J., Palmer, S., Rignot, E., Steinhage, D., 2013. A new bed elevation dataset for Greenland. Cryosphere 7 (2), 499–510. http://dx.doi.org/10.5194/tc-7-499-2013.

Behrendt, J.C., 1999. Crustal and lithospheric structure of the West Antarctic Rift System from geophysical investigations – a review. Glob. Planet. Change 23 (1–4), 25–44. http://dx.doi.org/10.1016/S0921-8181(99)00049-1.

Bindschadler, R.A., Nowicki, S., Abe-Ouchi, A., Aschwanden, A., Choi, H., Fastook, J., Granzow, G., Greve, R., Gutowski, G., Herzfeld, U., Jackson, C., Johnson, J., Khroulev, C., Levermann, A., Lipscomb, W.H., Martin, M.A., Morlighem, M., Parizek, B.R., Pollard, D., Price, S.F., Ren, D., Saito, F., Sato, T., Seddik, H., Seroussi, H., Takahashi, K., Walker, R., Wang, W.L., 2013. Ice-sheet model sensitivities to environmental forcing and their use in projecting future sea level (the SeaRISE project). J. Glaciol. 59 (214), 195–224. http://dx.doi.org/10.3189/2013JoG12J125.

Clark, J.A., Lingle, C.S., 1977. Future sea-level changes due to West Antarctic ice sheet fluctuations. Nature 269 (5625), 206–209. http://dx.doi.org/10.1038/269206a0.

Comiso, J.C., 2000. Variability and trends in Antarctic surface temperatures from in situ and satellite infrared measurements. J. Climate 13 (10), 1674–1696. http://dx.doi.org/10.1175/1520-0442(2000)013<1674:VATIAS>2.0.CO;2.

Crucifix, M., Loutre, M., Lambeck, K., Berger, A., 2001. Effect of isostatic rebound on modeled ice volume variations during the last 200 kyr. Earth Planet. Sci. Lett. 184 (3–4), 623–633. http://dx.doi.org/10.1016/S0012-821X(00)00361-7.

de Boer, B., Stocchi, P., van de Wal, R.S.W., 2014. A fully coupled 3-D ice-sheet – sea-level model: algorithm and applications. Geosci. Model Dev. Discuss. 7 (3), 3505–3544. http://dx.doi.org/10.5194/gmdd-7-3505-2014.

Dziewonski, A.M., Anderson, D.L., 1981. Preliminary reference Earth model. Phys. Earth Planet. Inter. 25 (4), 297–356. http://dx.doi.org/10.1016/0031-9201(81)90046-7.

Farrell, W., Clark, J., 1976. On postglacial sea level. Geophys. J. Astron. Soc. 46, 647–667. http://dx.doi.org/10.1111/j.1365-246X.1976.tb01252.x.

Favier, L., Durand, G., Cornford, S.L., Gudmundsson, G.H., Gagliardini, O., Gillet-Chaulet, F., Zwinger, T., Payne, A.J., Le Brocq, A.M., 2014. Retreat of Pine Island Glacier controlled by marine ice-sheet instability. Nature Clim. Change 4 (2), 117–121. http://dx.doi.org/10.1038/nclimate2094.

Foldvik, A., Kvinge, T., 1974. Conditional instability of sea water at the freezing point. Deep-Sea Res. 21 (3), 169–174. http://dx.doi.org/10.1016/0011-7471(74)90056-4.

Fretwell, P., Pritchard, H.D., Vaughan, D.G., Bamber, J.L., Barrand, N.E., Bell, R., Bianchi, C., Bingham, R.G., Blankenship, D.D., Casassa, G., Catania, G., Callens, D., Conway, H., Cook, A.J., Corr, H.F.J., Damaske, D., Damm, V., Ferraccioli, F., Forsberg, R., Fujita, S., Gim, Y., Gogineni, P., Griggs, J.A., Hindmarsh, R.C.A., Holmlund, P., Holt, J.W., Jacobel, R.W., Jenkins, A., Jokat, W., Jordan, T., King, E.C., Kohler, J., Krabill, W., Riger-Kusk, M., Langley, K.A., Leitchenkov, G., Leuschen, C., Luyendyk, B.P., Matsuoka, K., Mouginot, J., Nitsche, F.O., Nogi, Y., Nost, O.A., Popov, S.V., Rignot, E., Rippin, D.M., Rivera, A., Roberts, J., Ross, N., Siegert, M.J., Smith, A.M., Steinhage, D., Studinger, M., Sun, B., Tinto, B.K., Welch, B.C., Wilson, D., Young, D.A., Xiangbin, C., Zirizzotti, A., 2013. Bedmap2: improved ice bed, surface and thickness datasets for Antarctica. Cryosphere 7 (1), 375–393. http://dx.doi.org/10.5194/tc-7-375-2013.

Frieler, K., Clark, P.U., He, F., Buizert, C., Reese, R., Ligtenberg, S.R.M., van den Broeke, M.R., Winkelmann, R., Levermann, A., 2015. Consistent evidence of increasing Antarctic accumulation with warming. Nature Clim. Change 5 (4), 348–352. http://dx.doi.org/10.1038/nclimate2574.

Gomez, N., Mitrovica, J.X., Huybers, P., Clark, P.U., 2010. Sea level as a stabilizing factor for marine-ice-sheet grounding lines. Nat. Geosci. 3 (12), 850–853. http://dx.doi.org/10.1038/ngeo1012.

Gomez, N., Pollard, D., Mitrovica, J.X., Huybers, P., Clark, P.U., 2012. Evolution of a coupled marine ice sheet–sea level model. J. Geophys. Res. 117, F01013. http://dx.doi.org/10.1029/2011JF002128.

Gomez, N., Pollard, D., Mitrovica, J.X., 2013. A 3-D coupled ice sheet – sea level model applied to Antarctica through the last 40 kyr. Earth Planet. Sci. Lett. 384, 88–99. http://dx.doi.org/10.1016/j.epsl.2013.09.042.

Groh, A., Ewert, H., Scheinert, M., Fritsche, M., Rülke, A., Richter, A., Rosenau, R., Dietrich, R., 2012. An investigation of glacial isostatic adjustment over the Amundsen Sea sector, West Antarctica. Glob. Planet. Change 98–99, 45–53. http://dx.doi.org/10.1016/j.gloplacha.2012.08.001.

Gudmundsson, G.H., 2013. Ice-shelf buttressing and the stability of marine ice sheets. Cryosphere 7 (2), 647–655. http://dx.doi.org/10.5194/tc-7-647-2013.

Hagedoorn, J.M., Wolf, D., Martinec, Z., 2007. An estimate of global mean sea-level rise inferred from tide-gauge measurements using glacial-isostatic models consistent with the relative sea-level record. Pure Appl. Geophys. 164 (4), 791–818. http://dx.doi.org/10.1007/s00024-007-0186-7.

Hillenbrand, C., Kuhn, G., Smith, J.A., Gohl, K., Graham, A.G.C., Larter, R.D., Klages, J.P., Downey, R., Moreton, S.G., Forwick, M., Vaughan, D.G., 2013. Grounding-line retreat of the West Antarctic ice sheet from inner Pine Island Bay. Geology 41 (1), 35–38. http://dx.doi.org/10.1130/G33469.1.

Huybrechts, P., Oerlemans, J., 1990. Response of the Antarctic ice sheet to future greenhouse warming. Clim. Dyn. 5 (2), 93–102. http://dx.doi.org/10.1007/BF00207424.

Ivins, E.R., Sammis, C.G., 1995. On lateral viscosity contrast in the mantle and the rheology of low-frequency geodynamics. Geophys. J. Int. 123 (2), 305–322. http://dx.doi.org/10.1111/j.1365-246X.1995.tb06856.x.

Ivins, E.R., James, T.S., Wahr, J., Schrama, E.J.O., Landerer, F.W., Simon, K.M., 2013. Antarctic contribution to sea level rise observed by GRACE with improved GIA correction. J. Geophys. Res. 118 (6), 3126–3141. http://dx.doi.org/10.1002/jgrb.50208.

Joughin, I., Alley, R.B., 2011. Stability of the West Antarctic ice sheet in a warming world. Nat. Geosci. 4 (8), 506–513. http://dx.doi.org/10.1038/ngeo1194.

Kaufmann, G., Wu, P., Ivins, E.R., 2005. Lateral viscosity variations beneath Antarctica and their implications on regional rebound motions and seismotectonics. J. Geodyn. 39 (2), 165–181. http://dx.doi.org/10.1016/j.jog.2004.08.009.

King, M.A., Bingham, R.J., Moore, P., Whitehouse, P.L., Bentley, M.J., Milne, G.A., 2012. Lower satellite-gravimetry estimates of Antarctic sea-level contribution. Nature 491, 586–589. http://dx.doi.org/10.1038/nature11621.

Klemann, V., Martinec, Z., Ivins, E.R., 2008. Glacial isostasy and plate motion. J. Geodyn. 46 (3–5), 95–103. http://dx.doi.org/10.1016/j.jog.2008.04.005.

Konrad, H., Thoma, M., Sasgen, I., Klemann, V., Barbi, D., Grosfeld, K., Martinec, Z., 2014. The deformational response of a viscoelastic solid earth model coupled to a thermomechanical ice sheet model. Surv. Geophys. 35 (6), 1441–1458. http://dx.doi.org/10.1007/s10712-013-9257-8.

Le Meur, E., Huybrechts, P., 1996. A comparison of different ways of dealing with isostasy: examples from modeling the Antarctic ice sheet during the last glacial cycle. Ann. Glaciol. 23, 309–317.

Levitus, S., Antonov, J.I., Boyer, T.P., Baranova, O.K., Garcia, H.E., Locarnini, R.A., Mishonov, A.V., Reagan, J.R., Seidov, D., Yarosh, E.S., Zweng, M.M., 2012. World ocean heat content and thermosteric sea level change (0–2000 m), 1955–2010. Geophys. Res. Lett. 39 (10). http://dx.doi.org/10.1029/2012GL051106.

Ligtenberg, S.R.M., van de Berg, W.J., van den Broeke, M.R., Rae, J.G.L., van Meijgaard, E., 2013. Future surface mass balance of the Antarctic ice sheet and its influence on sea level change, simulated by a regional atmospheric climate model. Clim. Dyn. 41 (3–4), 867–884. http://dx.doi.org/10.1007/s00382-013-1749-1.

Lough, A.C., Wiens, D.A., Grace Barcheck, C., Anandakrishnan, S., Aster, R.C., Blankenship, D.D., Huerta, A.D., Nyblade, A., Young, D.A., Wilson, T.J., 2013. Seismic detection of an active subglacial magmatic complex in Marie Byrd Land, Antarctica. Nat. Geosci. 6 (12), 1031–1035. http://dx.doi.org/10.1038/ngeo1992.

Martin, M.A., Winkelmann, R., Haseloff, M., Albrecht, T., Bueler, E., Khroulev, C., Levermann, A., 2011. The Potsdam Parallel Ice Sheet Model (PISM-PIK) – part 2: dynamic equilibrium simulation of the Antarctic ice sheet. Cryosphere 5 (3), 727–740. http://dx.doi.org/10.5194/tc-5-727-2011.

Martinec, Z., 2000. Spectral-finite element approach to three-dimensional viscoelastic relaxation in a spherical Earth. Geophys. J. Int. 142 (1), 117–141. http://dx.doi.org/10.1046/j.1365-246x.2000.00138.x.

Mercer, J.H., 1968. Antarctic ice and Sangamon sea level. In: IAHS Publications – Red Books, vol. 79, pp. 217–225. http://iahs.info/uploads/dms/079020.pdf.

Mitrovica, J.X., Milne, G.A., 2003. On post-glacial sea level: I. General theory. Geophys. J. Int. 154 (2), 253–267. http://dx.doi.org/10.1046/j.1365-246X.2003.01942.x.

Mitrovica, J.X., Wahr, J., 2011. Ice Age Earth rotation. Annu. Rev. Earth Planet. Sci. 39 (1), 577–616. http://dx.doi.org/10.1146/annurev-earth-040610-133404.

Morelli, A., Danesi, S., 2004. Seismological imaging of the Antarctic continental lithosphere: a review. Glob. Planet. Change 42 (1–4), 155–165. http://dx.doi.org/10.1016/j.gloplacha.2003.12.005.

Nield, G.A., Whitehouse, P.L., King, M.A., Clarke, P.J., Bentley, M.J., 2012. Increased ice loading in the Antarctic Peninsula since the 1850s and its effect on glacial isostatic adjustment. Geophys. Res. Lett. 39 (17). http://dx.doi.org/10.1029/2012GL052559.

Oppenheimer, M., 1998. Global warming and the stability of the West Antarctic ice sheet. Nature 393 (6683), 325–332. http://dx.doi.org/10.1038/30661.

Pattyn, F., Perichon, L., Durand, G., Favier, L., Gagliardini, O., Hindmarsh, R.C.A., Zwinger, T., Albrecht, T., Cornford, S., Docquier, D., Fürst, J.J., Goldberg, D., Gudmundsson, G.H., Humbert, A., Hütten, M., Huybrechts, P., Jouvet, G., Kleiner, T., Larour, E., Martin, D., Morlighem, M., Payne, A.J., Pollard, D., Rückamp, M., Rybak, O., Seroussi, H., Thoma, M., Wilkens, N., 2013. Grounding-line migration in plan-view marine ice-sheet models: results of the ice2sea MISMIP3d intercomparison. J. Glaciol. 59 (215), 410–422. http://dx.doi.org/10.3189/2013JoG12J129.

Paulsen, T., Wilson, T.J., 2004. Subglacial bedrock structure in the transantarctic mountains and its influence on ice sheet flow: insights from {RADARSAT} {SAR} imagery. Glob. Planet. Change 42 (1–4), 227–240. http://dx.doi.org/10.1016/j.gloplacha.2003.12.004.

Peltier, W.R., 1974. The impulse response of a Maxwell Earth. Rev. Geophys. 12 (4), 649–669. http://dx.doi.org/10.1029/RG012i004p00649.

Pollard, D., DeConto, R.M., 2012a. A simple inverse method for the distribution of basal sliding coefficients under ice sheets, applied to Antarctica. Cryosphere 6 (5), 953–971. http://dx.doi.org/10.5194/tc-6-953-2012.

Pollard, D., DeConto, R.M., 2012b. Description of a hybrid ice sheet-shelf model, and application to Antarctica. Geosci. Model Dev. 5 (5), 1273–1295. http://dx.doi.org/10.5194/gmd-5-1273-2012.

Pollard, D., DeConto, R.M., Alley, R.B., 2015. Potential Antarctic ice sheet retreat driven by hydrofracturing and ice cliff failure. Earth Planet. Sci. Lett. 412, 112–121. http://dx.doi.org/10.1016/j.epsl.2014.12.035.

Rignot, E., Mouginot, J., Morlighem, M., Seroussi, H., Scheuchl, B., 2014. Widespread, rapid grounding line retreat of Pine Island, Thwaites, Smith, and Kohler glaciers, West Antarctica, from 1992 to 2011. Geophys. Res. Lett. 41 (10), 3502–3509. http://dx.doi.org/10.1002/2014GL060140.

Robinson, A., Calov, R., Ganopolski, A., 2012. Multistability and critical thresholds of the Greenland ice sheet. Nature Clim. Change 2 (6), 429–432. http://dx.doi.org/10.1038/nclimate1449.

Scherer, R.P., Aldahan, A., Tulaczyk, S., Possnert, G., Engelhardt, H., Kamb, B., 1998. Pleistocene Collapse of the West Antarctic ice sheet. Science 281 (5373), 82–85. http://dx.doi.org/10.1126/science.281.5373.82.

Schoof, C., 2007. Ice sheet grounding line dynamics: steady states, stability, and hysteresis. J. Geophys. Res. 112 (F3). http://dx.doi.org/10.1029/2006JF000664.

Shepherd, A., Ivins, E.R., A, G., Barletta, V.R., Bentley, M.J., Bettadpur, S., Briggs, K.H., Bromwich, D.H., Forsberg, R., Galin, N., Horwath, M., Jacobs, S., Joughin, I., King, M.A., Lenaerts, J.T.M., Li, J., Ligtenberg, S.R.M., Luckman, A., Luthcke, S.B., McMillan, M., Meister, R., Milne, G., Mouginot, J., Muir, A., Nicolas, J.P., Paden, J., Payne, A.J., Pritchard, H., Rignot, E., Rott, H., Sandberg Sörensen, L., Scambos, T.A., Scheuchl, B., Schrama, E.J.O., Smith, B., Sundal, A.V., van Angelen, J.H., van de Berg, W.J., van den Broeke, M.R., Vaughan, D.G., Velicogna, I., Wahr, J., Whitehouse, P.L., Wingham, D.J., Yi, D., Young, D., Zwally, H.J., 2012. A reconciled estimate of ice-sheet mass balance. Science 338 (6111), 1183–1189. http://dx.doi.org/10.1126/science.1228102.

Sutterley, T.C., Velicogna, I., Rignot, E., Mouginot, J., Flament, T., van den Broeke, M.R., van Wessem, J.M., Reijmer, C.H., 2014. Mass loss of the Amundsen Sea Embayment of West Antarctica from four independent techniques. Geophys. Res. Lett. http://dx.doi.org/10.1002/2014GL061940.

Thoma, M., Jenkins, A., Holland, D., Jacobs, S., 2008. Modelling circumpolar deep water intrusions on the Amundsen sea continental shelf, Antarctica. Geophys. Res. Lett. 35 (18). http://dx.doi.org/10.1029/2008GL034939.

Thomas, R.H., Bentley, C.R., 1978. A model for Holocene retreat of the West Antarctic ice sheet. Quat. Res. 10 (2), 150–170. http://dx.doi.org/10.1016/0033-5894(78)90098-4.

Timmermann, R., Hellmer, H.H., 2013. Southern Ocean warming and increased ice shelf basal melting in the twenty-first and twenty-second centuries based on coupled ice–ocean finite-element modeling. Ocean Dyn. 63 (9–10), 1011–1026. http://dx.doi.org/10.1007/s10236-013-0642-0.

van de Berg, W.J., van den Broeke, M.R., Reijmer, C.H., van Meijgaard, E., 2006. Reassessment of the Antarctic surface mass balance using calibrated output of a regional atmospheric climate model. J. Geophys. Res. 111, D11104. http://dx.doi.org/10.1029/2005JD006495.

van den Berg, J., van de Wal, R.S.W., Milne, G.A., Oerlemans, J., 2008. Effect of isostasy on dynamical ice sheet modeling: a case study for Eurasia. J. Geophys. Res. 113, B05412. http://dx.doi.org/10.1029/2007JB004994.

van der Wal, W., Whitehouse, P.L., Schrama, E.J.O., 2015. Effect of GIA models with 3D composite mantle viscosity on GRACE mass balance estimates for Antarctica. Earth Planet. Sci. Lett. 414, 134–143. http://dx.doi.org/10.1016/j.epsl.2015.01.001.

Weertman, J., 1957. On the sliding of glaciers. J. Glaciol. 3 (21), 33–38.

Whitehouse, P.L., Bentley, M.J., Milne, G.A., King, M.A., Thomas, I.D., 2012. A new glacial isostatic adjustment model for Antarctica: calibrated and tested using observations of relative sea-level change and present-day uplift rates. Geophys. J. Int. 190 (3), 1464–1482. http://dx.doi.org/10.1111/j.1365-246X.2012.05557.x.